



**HAL**  
open science

# Olivine intergranular plasticity at mantle pressures and temperatures

Paul Raterron, Caroline Bollinger, Sébastien Merkel

► **To cite this version:**

Paul Raterron, Caroline Bollinger, Sébastien Merkel. Olivine intergranular plasticity at mantle pressures and temperatures. *Comptes Rendus Géoscience*, 2019, *Comptes Rendus Geoscience*, 351 (2-3), pp.80-85. 10.1016/j.crte.2018.10.001 . hal-02168201

**HAL Id: hal-02168201**

**<https://hal.univ-lille.fr/hal-02168201v1>**

Submitted on 22 Oct 2021

**HAL** is a multi-disciplinary open access archive for the deposit and dissemination of scientific research documents, whether they are published or not. The documents may come from teaching and research institutions in France or abroad, or from public or private research centers.

L'archive ouverte pluridisciplinaire **HAL**, est destinée au dépôt et à la diffusion de documents scientifiques de niveau recherche, publiés ou non, émanant des établissements d'enseignement et de recherche français ou étrangers, des laboratoires publics ou privés.



Distributed under a Creative Commons Attribution - NonCommercial - NoDerivatives 4.0 International License

1 **Olivine intergranular plasticity at mantle pressures and temperatures**

2 Paul Raterron\*, Caroline Bollinger<sup>†</sup>, Sébastien Merkel

3 Unité Matériaux et Transformation (UMET), CNRS, Université Lille 1, F-59655 Villeneuve  
4 d'Ascq Cedex, France.

5

6 \*Corresponding author, presently at National Science Foundation, 2415 Eisenhower Avenue,  
7 Alexandria, VA 22314, USA; praterro@nsf.gov

8 <sup>†</sup> Now at: Bayerisches Geoinstitut, University of Bayreuth, 95440 Bayreuth, Germany

9

10

11 **Key points:**

12 We quantify the strain accommodated by grain-to-grain interactions in olivine aggregates.

13 Our results demonstrate that intergranular plasticity is dominant at mantle pressure.

14 Olivine strength in the mantle may be lower than predicted by classical flow laws.

15           **Abstract**

16           The ductile behavior of olivine-rich rocks is critical to constrain thermal convection in  
17 the Earth's upper mantle. Classical olivine flow laws for dislocation or diffusion creep fail to  
18 explain the fast post-seismic surface displacements observed by GPS, which requires a much  
19 weaker lithosphere than predicted by classical laws. Here we compare the plasticity of olivine  
20 aggregates deformed experimentally at mantle pressures and temperatures to that of single  
21 crystals and demonstrate that, depending on conditions of stress and temperature, strain  
22 accommodated through grain-to-grain interactions - here called intergranular strain - can be  
23 orders of magnitude larger than intracrystalline strain, which significantly weakens olivine  
24 strength. This result, extrapolated along mantle geotherms suggests that intergranular  
25 plasticity could be dominant in most of the upper mantle. Consequently, the strength of  
26 olivine-rich aggregates in the upper mantle may be significantly lower than predicted by flow  
27 laws based on intracrystalline plasticity models.

## 28           **1. Introduction**

29           The plasticity of olivine-rich rocks constraints that of Earth's upper mantle.  
30           Consequently, there has been considerable effort to quantify olivine aggregate rheology in  
31           terms of flow laws which can be implemented in geodynamical models for mantle thermal  
32           convection. Experimental studies investigated the effects of temperature and stress [a review  
33           in *Hirth and Kohlstedt*, 2003], pressure [e.g., *Durham et al.*, 2009; *Hilaireret et al.*, 2012;  
34           *Bollinger et al.*, 2013], fluid fugacities [e.g., *Kohlstedt*, 2006; *Keefner et al.*, 2011; *Ohuchi et al.*  
35           *et al.*, 2017], grain size [*Warren and Hirth*, 2006], lattice preferred orientations [e.g., *Hansen et al.*  
36           *et al.*, 2013] and melt fractions [e.g., *Hirth and Kohlstedt*, 1995]. The traditional view is to  
37           assign one dominant deformation mechanism to given deformation conditions [*Frost and*  
38           *Ashby*, 1982] and implement the flow law with specific dependences on temperature, stress or  
39           grain size. At the microscopic scale, however, olivine aggregate plasticity involves numerous  
40           mechanisms operating concurrently, within the grains and at grain boundary (Fig. 1). To this  
41           day, the fundamental question of the amount of strain accommodated in the mantle through  
42           grain-to-grain interactions versus that accommodated within the grain remains unanswered.

43           Strain accommodation at grain boundary has been attributed to several distinct  
44           mechanisms. A model for the deformation of aggregates by grain-boundary diffusion was  
45           introduced by *Coble* [1963] to explain the high-temperature plasticity of alumina. Coble  
46           creep requires the rearrangement of grain interfaces by grain-boundary sliding (GBS). The  
47           corresponding flow law exhibits a linear dependence on stress and a strong inverse  
48           dependence on grain size ( $d$ ), theoretically to the power  $p = -3$ . For persistently small grain  
49           sizes - when grain growth is for example impeded by Zener pinning - Coble creep may  
50           contribute to superplastic flow, which has been characterized at room pressure in olivine rich  
51           aggregates [e.g., *Hiraga et al.*, 2010]. Grain-boundary sliding can also be assisted by  
52           dislocation motions within grains, which contribute to relax stress concentration at triple

53 junctions. This mechanism, called dislocation-assisted grain boundary sliding (disGBS), has  
54 been observed at low pressure in olivine [*Hirth and Kohlstedt, 2003; Hansen et al., 2011*]. It  
55 is characterized by a strain rate depending strongly on stress, typically to the power  $n \sim 3$ ,  
56 with an inverse dependence on grain size to a power  $p$  within  $[-2, -0.6]$ . Other deformation  
57 mechanisms, which do not exist in single crystals, accommodate strain in olivine aggregates.  
58 Motions of disclinations - defects identified along grain boundaries in olivine [*Cordier et al.,*  
59 *2014*] - can accommodate strain. Furthermore, interactions between grains, in materials with  
60 limited number of intracrystalline deformation mechanisms, generate locally high stress  
61 concentration [e.g., *Castelnau et al., 2008*]. In materials with anisotropic elastic and plastic  
62 properties such as olivine this may promote high stress and strain transmission patterns  
63 percolating throughout the aggregates [*Burnley, 2013*]. Conversely, the stress field associated  
64 with single-crystal deformation can only be relaxed by intracrystalline deformation  
65 mechanisms, such as dislocation motions (glide, climb and cross slip) and intracrystalline  
66 diffusion (e.g., Nabarro-Herring diffusion).

67       Recently, *Tielke et al.* [2016] compared olivine single-crystal and aggregate high-  
68 temperature rheology at low pressure, and quantified the contribution of both intracrystalline  
69 and intergranular mechanisms to the aggregate strain. They determine that olivine aggregates  
70 deform up to 4.6 times faster than what would be expected assuming only intracrystalline  
71 plasticity; the latter's contribution to strain rate was calculated from micromechanical  
72 modeling of dislocations activity. Following a similar approach, we here compare olivine  
73 single-crystal and aggregate high-temperature plasticity, as measured experimentally at the  
74 high pressures representative of mantle conditions. We demonstrate that grain-to-grain  
75 interactions significantly contribute to accommodating strain in experiments. Extrapolation to  
76 mantle stress conditions along geotherms suggests that intergranular plasticity may also  
77 dominate upper mantle plasticity.

78

## 79 **2. Methods: intracrystalline vs intergranular plasticity**

80 Comparing aggregates and single-crystal deformation data allows quantifying the  
81 strain rate contributions of intergranular deformation mechanisms. Assuming that  
82 intracrystalline (IC) and intergranular (IG) mechanisms operate concurrently, we have:

$$83 \quad \dot{\epsilon}_{\text{Agg}} = \dot{\epsilon}_{\text{IC}} + \dot{\epsilon}_{\text{IG}} \quad (1),$$

84 where  $\dot{\epsilon}_{\text{Agg}}$  is the strain rate of the aggregate,  $\dot{\epsilon}_{\text{IC}}$  is the contribution of intracrystalline  
85 processes and  $\dot{\epsilon}_{\text{IG}}$  is due to grain-to-grain interactions. The plasticity of aggregates can thus be  
86 quantified by introducing the following ratio:

$$87 \quad \dot{\epsilon}_{\text{Agg}}/\dot{\epsilon}_{\text{IC}} = 1 + \dot{\epsilon}_{\text{IG}}/\dot{\epsilon}_{\text{IC}} \quad (2),$$

88 It should range from 1, when all the aggregate strain is accommodated within the grains, to  
89  $+\infty$ , when the strain is fully accommodated through grain-to-grain deformation processes.  
90 Values for  $\dot{\epsilon}_{\text{Agg}}$  and  $\dot{\epsilon}_{\text{IC}}$  (and their ratio  $\dot{\epsilon}_{\text{Agg}}/\dot{\epsilon}_{\text{IC}}$ ) can be directly extracted from previously  
91 published rheological data (Figure 2).

92 We used  $\dot{\epsilon}_{\text{Agg}}$  values for San Carlos olivine aggregates deformed in axisymmetric  
93 compression at mantle pressure and temperature in the Deformation-DIA (D-DIA) apparatus,  
94 as reported by *Durham et al.* [2009], *Hilairiet et al.* [2012] and *Bollinger et al.* [2013]  
95 (supplementary Table S1). For each  $\dot{\epsilon}_{\text{Agg}}$  reported value, the corresponding  $\dot{\epsilon}_{\text{IC}}$  can be  
96 calculated at identical pressure ( $P$ ), temperature ( $T$ ) and differential stress ( $\sigma$ ) by combining  
97 experimental flow laws for San Carlos olivine single crystals [*Mackwell et al.*, 1985; *Bai et*  
98 *al.*, 1991, *Raterron et al.*, 2009, 2012; *Girard et al.*, 2013] (supplementary materials, Table  
99 S2). Indeed, assuming homogeneous stress throughout the aggregate (lower bound approach,

100 i.e. Sachs' bound) - one of the simplest end-member assumption when analytically addressing  
101 aggregate strain - and random grain orientations in the aggregate,  $\dot{\epsilon}_{IC}$  reads:

$$102 \quad \dot{\epsilon}_{IC} = 0.123 (\dot{\epsilon}_{[110]c} + \dot{\epsilon}_{[011]c} + \dot{\epsilon}_{[101]c}) \quad (3),$$

103 where  $\dot{\epsilon}_{[110]c}$ ,  $\dot{\epsilon}_{[011]c}$ , and  $\dot{\epsilon}_{[101]c}$  are the strain rates of oriented single crystals and the  
104 0.123 geometrical factor arises from averaging over crystal orientations [Raterron *et al.*,  
105 2011]. The indexes indicate the crystallographic orientation of the compression direction –  
106 e.g., [110]<sub>c</sub> direction is at 45° angle from [100] and [010] directions. [110]<sub>c</sub>, [011]<sub>c</sub>, [101]<sub>c</sub>  
107 promote respectively [100](010) dislocation slip, [001](010) dislocation slip, and [100](001)  
108 and [001](100) slips together. The single-crystal strain rates  $\dot{\epsilon}_{[110]c}$ ,  $\dot{\epsilon}_{[011]c}$ , and  $\dot{\epsilon}_{[101]c}$   
109 account for pressure, temperature, water content, and oxygen fugacity ( $fO_2$ ) and are based on  
110 data from the literature (Supplementary information). For the dry experiments reported by  
111 *Durham et al.* [2009] (squares in Fig. 2), we assumed a dry-crystal rheology when calculating  
112  $\dot{\epsilon}_{IC}$ ; for the wet experiments reported by *Hilaireret et al.* [2012] and *Bollinger et al.* [2013]  
113 (triangles and circles in Fig. 2), we assumed wet-crystal rheology.  $\dot{\epsilon}_{IC}$  was also calculated  
114 assuming oxygen fugacity conditions comparable to those of the experiments. For *Durham et*  
115 *al.*'s [2009] experiments, where the Ni/NiO buffer controlled  $fO_2$ , we assumed the Ni/NiO  
116 buffer oxygen fugacity [Frost, 1991]. For the unbuffered experiments [*Hilaireret et al.*, 2012;  
117 *Bollinger et al.*, 2013] - where oxygen fugacity was not controlled but specimens were placed  
118 within a boron nitride sleeve which promotes low  $fO_2$  conditions [*Wendland et al.*, 1985] - we  
119 assumed the oxygen fugacity of the iron-wüstite buffer (IW) which borders the olivine  
120 stability field.

### 121 **3. Results: aggregate strain rate $\dot{\epsilon}_{Agg}$ versus intracrystalline strain rate $\dot{\epsilon}_{IC}$**

122 Figure 2.a shows the aggregate strain rate  $\dot{\epsilon}_{Agg}$ , as measured experimentally (Table  
123 S1), versus the intracrystalline strain rate  $\dot{\epsilon}_{IC}$  (Eq. 3) calculated at identical  $P$ ,  $T$  and  $\sigma$ .

124 Because of our initial assumption (Sachs' bound), Eq. 3 tends to overestimate the  
125 intracrystalline strain rate. This may occasionally lead to  $\dot{\epsilon}_{\text{Agg}} < \dot{\epsilon}_{\text{IC}}$  when strain is fully  
126 accommodated by intracrystalline processes. Remarkably, we have  $\dot{\epsilon}_{\text{Agg}} \geq \dot{\epsilon}_{\text{IC}}$  (within  
127 uncertainty) for all but one experimental point, by factors reaching  $\sim 20$  at 1673 K and  $\sim 2000$   
128 at 1373 K. This shows that, in high-pressure deformation experiments, *i*) a significant  
129 fraction of aggregate strain is accommodated by mechanisms involving grain-to-grain  
130 interactions, even in regimes where dislocation creep was observed. It also shows that *ii*) this  
131 fraction tends to increase with decreasing temperature. Also show on Figure 2.a are the data  
132 reported by Tielke et al. (2016) obtained at low pressure (open diamonds, green is for 1523  
133 K). For these data, shear strain rates and stresses were converted into compressional strain  
134 rates and stresses before plotting. Tielke et al. report that the aggregate strain rate is up to 4.6  
135 times higher than the intracrystalline strain rate as calculated using a micromechanical  
136 modeling; Figure 2.a shows that these data fall, indeed, in the vicinity of the line  
137 corresponding to a ratio of 4.6 between the measured strain rate and the intracrystalline strain  
138 rates calculated here using the analytical approach described above. It is remarkable that using  
139 two different approaches, Tielke et al. and we obtained similar results. This give us  
140 confidence in the analytical approach used here.

141 Figure 2.b shows  $\log(\dot{\epsilon}_{\text{Agg}}/\dot{\epsilon}_{\text{IC}})$  versus stress; the color code indicate approximate  
142 temperatures. The ratio  $\dot{\epsilon}_{\text{Agg}}/\dot{\epsilon}_{\text{IC}}$  varies over orders of magnitude, from  $\sim 1$  to  $\sim 2 \times 10^3$ . When  
143  $\dot{\epsilon}_{\text{Agg}}/\dot{\epsilon}_{\text{IC}} \sim 1$  the aggregate strain is fully accommodated within the grains, while  $\dot{\epsilon}_{\text{Agg}}/\dot{\epsilon}_{\text{IC}} \gg$   
144 2 indicates that strain is mostly accommodated by grain-to-grain interactions (intergranular  
145 mechanisms). Within our model, one should always satisfy  $\dot{\epsilon}_{\text{Agg}}/\dot{\epsilon}_{\text{IC}} \geq 1$  (Eq. 2) which,  
146 within uncertainties, is in agreement with most experimental data. At a given temperature,  
147  $\log(\dot{\epsilon}_{\text{Agg}}/\dot{\epsilon}_{\text{IC}})$  decreases with increasing differential stress (Fig. 2.b) until  $\log(\dot{\epsilon}_{\text{Agg}}/\dot{\epsilon}_{\text{IC}}) \sim 0$



148 is achieved, i.e. strain is fully accommodated within the grains ( $\dot{\epsilon}_{\text{Agg}} = \dot{\epsilon}_{\text{IC}}$ ). A further  
 149 increase of stress will have no effect on Eq. 2 ratios. This result is in agreement with the  
 150 conventional interpretation that increasing stress and strain rate at given temperature favors  
 151 dislocation creep [*Frost and Ashby, 1982*] - a grain-size insensitive creep involving mostly  
 152 intracrystalline plasticity - with respect to grain-size sensitive creep which involves  
 153 intergranular plasticity.

154 The contribution of grain-to-grain deformation processes to the aggregate strain also  
 155 decreases with temperature (Figs. 2a and 2.b). This effect may result from a combination of  
 156 factors, such as: an increasing aggregate grain size with temperature, i.e., a decreasing grain-  
 157 boundary surface/bulk volume ratio favoring intracrystalline deformation mechanisms; an  
 158 increasing activity of disclinations with decreasing  $T$  favoring intergranular plasticity; higher  
 159 stress and strain concentrations near grain boundaries at lower  $T$ , or a more effective stress  
 160 percolation at moderate  $T$  [*Burnley, 2012*] promoting high-strain networks throughout the  
 161 aggregates, accounted here for as intergranular strain.

162 A linear fit through  $\log(\dot{\epsilon}_{\text{Agg}}/\dot{\epsilon}_{\text{IC}})$  in Figure 2.b leads to the empirical equation:

$$163 \quad \log(\dot{\epsilon}_{\text{Agg}}/\dot{\epsilon}_{\text{IC}}) = 20.4 - 0.0115 T - 0.0045 \sigma \quad (4),$$

164 where  $T$  is in K, and the differential stress  $\sigma$  is in MPa.  $\dot{\epsilon}_{\text{Agg}}/\dot{\epsilon}_{\text{IC}}$  must remain  $\geq 1$ . Therefore,  
 165  $\dot{\epsilon}_{\text{Agg}}/\dot{\epsilon}_{\text{IC}} = 1$  is here imposed when Eq. 4 gives values  $< 1$ . Note that, although empirical,  
 166 Eq. 4 accounts for all dry and wet data with good consistency between studies. Combining  
 167 Eqs. 2 and 4, a first-order estimate of olivine aggregate strain rate can be calculated from the  
 168 intracrystalline strain rate  $\dot{\epsilon}_{\text{IC}}$  (Eq. 3) through the following composite flow law:

$$169 \quad \dot{\epsilon}_{\text{Agg}} = \text{Max}[1; 10^{(20.4 - 0.0115 T - 0.0045 \sigma)}] \times \dot{\epsilon}_{\text{IC}} \quad (5),$$

170 where  $\text{Max}[i; j]$  is the maximum of  $i$  and  $j$ ,  $T$  is in K and  $\sigma$  is in MPa. Note that the effects of  
 171 pressure, temperature, stress, oxygen fugacity, or hydrous conditions are accounted for in the

172 intracrystalline flow laws (Eq. 3, supplementary materials, Table S2). In the following, we  
173 explore the implications for the upper mantle of the effect of pressure and temperature on  
174 intracrystalline vs intergranular plasticity.

#### 175 **4. Discussion: Extrapolation to mantle conditions**

176 Figure 3.a shows  $\log(\dot{\epsilon}_{\text{Agg}}/\dot{\epsilon}_{\text{IC}})$  calculated along two oceanic geotherms (20-Ma and  
177 80-Ma) for a differential stress  $\sigma = 1$  MPa - i.e., a shear stress  $\mu = 1/\sqrt{3}$  MPa which is a  
178 reasonable value for the mid to deep upper mantle [Bürgmann and Dresen, 2008] - and along  
179 a classic continental geotherm (supplementary Fig. S1, see also Turcotte and Schubert [2002])  
180 for  $\sigma = 1$  and 50 MPa. The latter stress value is representative of shear zone in the coldest  
181 part of the lithosphere, and of experimental conditions. For this calculation, pressure was  
182 calculated with an upper-mantle average density of  $3.35 \text{ g/cm}^3$  (i.e. a  $32.9 \text{ MPa/km}$  vertical  
183 pressure gradient), and oxygen fugacity set at FMQ-2 which is reasonable for the upper  
184 mantle [Herd, 2008]. We assumed wet condition for this plot (supplementary materials).  
185 Figure 3.a suggests that, like in experiments, deformation in the upper mantle is largely  
186 accommodated by intergranular plasticity, especially in the cold lithosphere where grain-to-  
187 grain interactions may fully dominate olivine plasticity. This may promote a significant  
188 weakening of the aggregate with respect to the strength calculated from classical flow laws.

189 Figures 3.b shows the viscosity of olivine aggregate along oceanic (20 Ma, red curves)  
190 and continental (blue curves) geotherms, as calculated using the composite flow law of Eq. 5  
191 for a differential stress of 1 MPa. Wet conditions are assumed when using Eq. 5, as well as  
192 for plotting the Hirth and Kohlstedt [2003] dislocation creep flow law with hydroxyl content  
193  $C_{\text{OH}} = 300 \text{ ppm H/Si}$ . The intracrystalline strain rate calculated from Eq.3 is shown for  
194 comparison, together with two low-temperature flow laws [Raterron et al., 2004; Demouchy  
195 et al., 2013]. In both contexts, the composite flow law in Eq. 5 leads to viscosities about two

196 orders of magnitude lower than the *Hirth and Kohlstedt*'s dislocation creep flow law.  
197 Interestingly, in the shallow (cold) upper mantle, the composite flow law of Equation 5 is in  
198 relatively good agreement with the low-temperature flow laws reported for olivine, thus  
199 captures the change in rheology between high-temperature and low-temperature plasticity.  
200 Changing the differential stress to 50 MPa does not significantly affect these results  
201 (Supplemental Figure S2). At deeper depths (i.e. 400 km), the difference between the  
202 predictions of Eq. 5 and the dislocation creep law of *Hirth and Kohlstedt* [2003] is due to the  
203 pressure-induced change of dominant slip system in olivine [*Raterron et al.*, 2012].

204 It should be emphasized here that polycrystalline specimens in high-pressure experiments have  
205 small grain sizes, typically ranging from 1 to 50  $\mu\text{m}$ , which increases significantly their  
206 surface versus volume ratio when compared to that of mantle rocks with estimated grain sizes  
207 ranging from tenths of millimetre to centimetres. This enhances grain-to-grain interactions,  
208 hence intergranular plasticity, in laboratory specimens and may artificially lower their  
209 strength with respect to that of mantle rocks. The results reported here (Eq. 5 and Fig. 2) may,  
210 thus, significantly overestimate how much strain can be accommodated by grain-to-grain  
211 interactions in the coarse-grain mantle. However, our results may apply more directly in the  
212 context of mantle shear zones, where grain-size reduction weakens sheared peridotites  
213 (*Warren and Hirth*, 2006; *Skemer et al.*, 2011).

214 **5. Concluding remarks**

215 According to our results and extrapolation, we conclude that olivine strain is mostly  
216 accommodated by deformation mechanisms involving grain-to-grain interactions at mantle  
217 pressures and temperatures, which results in a much weaker strength as that obtained when  
218 combining single-crystal dislocation creep flow laws. Such a phenomenon was recently  
219 observed at low pressure [Tielke *et al.*, 2016], but is much more marked at high pressure  
220 where intergranular plasticity largely dominate deformation.

221 Uncertainties remain regarding the additional deformation mechanisms, present in  
222 aggregates and absent in single crystals, responsible for the measured low strength of  
223 aggregates with respect to that of single crystals. Several candidate mechanisms are  
224 mentioned in the introduction, such as disclinations, grain boundary sliding, stress/strain  
225 percolation, etc., but our analysis does not allow to favor one over another.

226 Furthermore, the empirical model presented here is extracted from deformation  
227 experiments carried out at high differential stresses on aggregates with small grain sizes  
228 compared to mantle conditions where stresses are much lower and grain sizes larger -.  
229 Further investigation is necessary to quantify the effects of increasing grain size and  
230 decreasing stress on Eq.4 parameters. As mentioned above, one may speculate that, due to the  
231 larger grain sizes, intracrystalline mechanisms may accommodate more strain in the Earth's  
232 mantle than in experiments and, hence, reduce the effect of grain-to-grain interactions  
233 highlighted here. Another source of discrepancy when extrapolating the present results to  
234 mantle processes is the presence of secondary phases such as pyroxenes, garnet and possibly  
235 partial melts in mantle peridotites which are absent in the present laboratory specimens.

236 Keeping in mind the above reservations, let us however emphasize that olivine  
237 classical flow laws, whether assuming dislocation or diffusion creep, fail to explain the fast  
238 surface displacement observed by GPS after large earthquakes [e.g., Freed *et al.*, 2010],

239 which requires a much weaker strength for the lithosphere, as the one we propose here. Also,  
240 the particularly deep weakening predicted here along a continental geotherm may provide an  
241 explanation for the elusiveness of the lithosphere-asthenosphere boundary beneath cratons  
242 [e.g., Eaton et al., 2009], since it should reduce the lithosphere-asthenosphere viscosity  
243 contrast. We thus conclude that grain-to-grain interactions are an important component of  
244 olivine plasticity at mantle pressures, and may likely contribute to the weakening of the  
245 Earth's upper mantle with respect to that calculated from classical flow laws for olivine.

246

247 **References**

- 248 Bai, Q., Mackwell, S.J., Kohlstedt, D.L. (1991) High-temperature creep of olivine single  
249 crystals.1. Mechanical results for buffered samples, *Journal of Geophysical Research* **96**,  
250 2441-2463.
- 251 Bollinger, C., Merkel, S., Raterron, P., Cordier, P. (2013) Olivine dislocation creep: revisiting  
252 experimental data to 8 GPa pressure, *Phys. Earth Planet. Int.* **228**, 211-219.
- 253 Burnley, P.C. (2013) The importance of stress percolation patterns in rocks and other  
254 polycrystalline materials, *Nature Communications* **4**:2117, doi: 10.1038/ncomms3117.
- 255 Bürgmann, R., Dresen, G. (2008) Rheology of the lower crust and upper mantle: evidence  
256 from rock mechanics, geodesy and field observations. *Annu. Rev. Earth Planet. Sci.* **36**,  
257 531–567.
- 258 Castelnau, O., Blackman, D.K., Lebensohn, R.A., Ponte Castañeda (2008) Micromechanical  
259 modeling of viscoplastic behavior of olivine, *J. Geophys. Res.* 113, B09202,  
260 doi:10.1029/2007JB005444.
- 261 Coble, R.L. (1963) A model for boundary diffusion controlled creep in polycrystalline  
262 materials, *J. Appl. Physics* **34** (6), 1679-1682.
- 263 Cordier, P., Demouchy, S., Beausir, B., Taupin, V., Barou, F., Fressengeas, C. (2014)  
264 Disclinations provide the missing mechanism for deforming olivine-rich rocks in the  
265 mantle, *Nature* **504**, 51-56, doi:10.1038/nature13043.
- 266 Demouchy, S., Tommasi, A., Boffa Ballaran, T., Cordier, P. (2013) Low strength of Earth's  
267 uppermost mantle inferred from tri-axial deformation experiments on dry olivine crystals,  
268 *Physics of the Earth and Planetary Interiors* **220**, 37-49.
- 269 Durham, W.B., Mei, S., Kohlstedt, D.L., Wang, L., Dixon, N.A. (2009) New measurement of  
270 activation volume in olivine under anhydrous conditions, *Phys. Earth Planet. Int.* **172**, 67-  
271 73.
- 272 Eaton, D.W., Darbshire, F., Evans, R.L., Grütter, H., Jones, A.G., Yuan, X. (2009) The  
273 elusive lithosphere-asthenosphere boundary (LAB) beneath cratons, *Lithos* **109**, 1-22.
- 274 Freed, A.M., Herring, T., Bürgmann, R. (2010) Steady-state laboratory flow laws alone fail to  
275 explain postseismic observations, *Earth and Planetary Science Letters* **300**, 1-10.
- 276 Frost, H.J., Ashby, M.F. (1982) "Deformation Mechanisms Maps: The Plasticity and Creep of  
277 Metals and Ceramics". 1st ed., Pergamon, Oxford; New York; Sydney.

278 Frost, B.R. (1991) Introduction to oxygen fugacity and its petrologic importance, in  
279 "Reviews in Mineralogy" Volume 25, *Oxide Minerals: Petrologic and Magnetic*  
280 *Significance*, D. H. Lindsley Ed., Mineralogical Society of America, New York, pp. 1-10.  
281 Girard, J. Chen, J., Raterron, P., Holyoke, C.W. III (2013) Hydrolytic weakening of olivine at  
282 mantle pressure: evidence of [100](010) slip system softening from single crystal  
283 deformation experiments, *Physics Earth Planet. Int.* **216**, 12-20.  
284 Hansen, L.N., Zimmerman, M.E., Kohlstedt, D.L. (2011) Grain boundary sliding in San  
285 Carlos olivine: Flow law parameters and crystallographic-preferred orientation, *Journal of*  
286 *Geophysical Research* **116**, B08201, doi:10.1029/2011JB008220.  
287 Hansen, L.N., Zimmerman, M.E., Kohlstedt, D.L. (2013) Laboratory measurements of  
288 viscous anisotropy of olivine aggregates, *Nature* **492**, 415-418.  
289 Herd, C.D.K. (2008) Basalts as probes of planetary interior redox state, *Rev. Mineral.*  
290 *Geochem.* **68**, 527-553.  
291 Hilairet, N., Wang, Y., Sanehira, T., Merkel, S., Mei, S. (2012) Deformation of olivine under  
292 mantle conditions: An in situ high-pressure, high-temperature study using monochromatic  
293 synchrotron radiation *Journal of Geophysical Research* **117**, B01203, doi:  
294 10.1029/2011JB008498.  
295 Hiraga, T., Miyazaki, T., Tasaka, M., Yoshida, H. (2010) Mantle superplasticity and its self-  
296 made demise, *Nature* **468**, 1091-1094, doi: 10.1038/nature09685.  
297 Hirth, G., Kohlstedt, D.L. (1995) Experimental constraints on the dynamics of partially  
298 molten upper mantle 2: deformation in the dislocation creep regime, *Journal of*  
299 *Geophysical Research* **100**, B8, 15441-15449.  
300 Hirth, G., Kohlstedt, D.L. (2003) Rheology of the upper mantle and the mantle wedge: a view  
301 from the experimentalists, in: Inside the Subduction Factory, *Geophys. Monogr. Ser.* **138**,  
302 J. Eiler (Ed.), AGU, Washington, D. C., pp. 83-105.  
303 Keefner, J.W., Mackwell, S. J., Kohlstedt, D. L., Heidelbach, F. (2011) Dependence of  
304 dislocation creep of dunite on oxygen fugacity: implications for viscosity variations in  
305 Earth's mantle, *Journal of Geophysical Research* **116**, B05201, doi:  
306 10.1029/2010JB007748.  
307 Kohlstedt, D.L. (2006) The role of water in high-temperature rock deformation, *Reviews in*  
308 *Mineralogy & Geochemistry* **62**, 377-396.  
309 Mackwell, S.J., Kohlstedt, D.L., Paterson, M.S. (1985) The role of water in the deformation  
310 of olivine single crystals, *Journal of Geophysical Research* **90**, 11319-11333.

311 Ohuchi, T., Kawazoe, T., Higo, Y., Suzuki, A. (2017) Flow behavior and microstructures of  
312 hydrous olivine aggregates at upper mantle pressures and temperatures, *Contrib. Mineral.*  
313 *Petrol.* **172**:65, doi: 10.1007/s00410-017-1375-8.

314 Raterron, P., Wu, Y., Weidner, D.J., Chen, J. (2004) Low temperature olivine rheology at  
315 high pressure, *Phys. Earth Planet. Int.* **145**, 149-159, doi:10.1016/j.pepi.2004.03.007.

316 Raterron, P., Amiguet, E., Chen, J., Li, L., Cordier, P. (2009) Experimental deformation of  
317 olivine single crystals at mantle pressure and temperature, *Phys. Earth Planet. Int.* **172**, 74-  
318 83.

319 Raterron, P., Girard, J., Chen, J. (2012) Activities of olivine slip systems in the upper mantle,  
320 *Phys. Earth Planet. Int.* **200-201**, 105-112.

321 Skemer, P., Sundberg, M., Hirth, G., Cooper, R. (2011) Torsion experiments on coarse-  
322 grained dunite: implications for microstructural evolution when diffusion creep is  
323 suppressed, Geological Society, London, Special publication 360, 211-233,  
324 doi:10.1144/SP360.12 .

325 Tielke, J.A., Hansen, L.N., Tasaka, M., Meyers, C., Zimmerman, M.E., Kohlstedt, D.L.  
326 (2016) Observation of grain size sensitive power law creep of olivine aggregates over a  
327 large range of lattice-preferred orientation strength, *J. Geophys. Res. Solid Earth* **121**, 506-  
328 516, doi:10.1002/2015JB012302.

329 Turcotte, D.L., Schubert, G. (2002) “*Geodynamics*”, Second Ed., Cambridge University  
330 Press, NY, USA, pp. 456.

331 Warren, J.M., Hirth, G. (2006) Grain size sensitive deformation mechanisms in naturally  
332 deformed peridotites, *Earth and Planetary Sciences Letters* **248**, 438-450.

333 Wendland, R.F., Huebner, J.S., Harrison, W.J. (1982) The redox potential of boron nitride and  
334 implications for its use as a crucible material in experimental petrology, *American*  
335 *Mineralogist* **67**, 170-174.

336

337



338 **Acknowledgements**

339 This research was supported by the Agence Nationale de la Recherche (ANR) Grant  
340 BLAN08-2\_343541 “Mantle Rheology”. We thank two anonymous reviewers for their  
341 thoughtful insights which helped improving the original manuscript. Part of the work was  
342 carried out while PR was serving at the National Science Foundation.

343 **Figure 1:** Schematics of mechanisms accommodating strain in olivine aggregates:  
344 dislocations (blue corners) glide, cross slip and climb within grains, disclinations (blue spirals,  
345 *Cordier et al.* [2014]) mostly active near grain boundaries, ionic diffusion (red arrows)  
346 occurring at grain interfaces (Cobble diffusion) or within the grains (Nabarro-Herring  
347 diffusion, dislocation climb), and grain-boundary sliding (green arrows, *Hansen et al.* [2011])  
348 which also involves diffusion and can be assisted by dislocations. Other mechanisms that do  
349 not accommodate strain, such as grain-boundary migration or recrystallization, also assist  
350 olivine deformation.

351

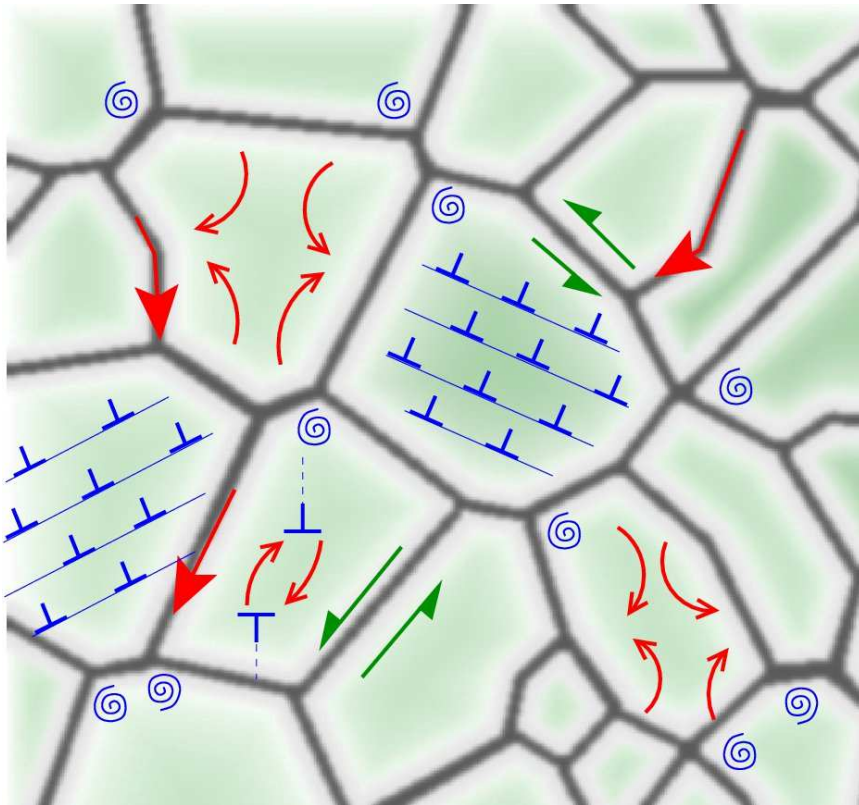
352 **Figure 2:** A) Aggregate strain rate  $\dot{\epsilon}_{\text{Agg}}$  as measured in experiments (Table S1) versus  
353 predictions based on intracrystalline strain rate  $\dot{\epsilon}_{\text{IC}}$  as calculated from Eq. 3 and Table S2  
354 parameters. The color code indicates experimental temperatures. D, H, and B are data from  
355 Durham et al. [2009], Hilairet et al. [2012], and Bollinger et al. [2013], respectively. Also  
356 show are the data reported by Tielke et al. [2016] (T; open diamond, green is for 1523K): for  
357 these data, shear strain rates and stresses were converted into compressional strain rates and  
358 stresses. The thick black line is identity, for which both strain rates are equal. Dotted and  
359 dashed lines indicate ratios for which the aggregate strain rate is 4.6 (dotted black), 19 (red),  
360 63 (orange), 281 (blue), and 1995 (dashed black) times faster than the intracrystalline strain  
361 rate. B)  $\log(\dot{\epsilon}_{\text{Agg}}/\dot{\epsilon}_{\text{IC}})$  versus experimental differential stress; the colored lines are the results  
362 of a bilinear fit in  $T$  and  $\sigma$  through the data (Eq. 4); their color indicate temperature.

363 **Figure 3:** A) ratio of the aggregate strain rate by the intracrystalline strain rate ( $\dot{\epsilon}_{\text{Agg}}/\dot{\epsilon}_{\text{IC}}$ )  
364 versus depth, as calculated from Eq.4 assuming no effect of grain size, along 20-Ma (red) and  
365 80-Ma (orange) oceanic geotherms, and a continental geotherm (blue) with a differential  
366 stress  $\sigma = 1$  MPa (solid lines) and 50 MPa (dashed line). B) Olivine aggregate dynamic  
367 viscosity as calculated along a 20-Ma oceanic geotherm (red lines) and a continental geotherm  
368 (blue lines) at 1 MPa stress and indicated conditions. The solid lines were obtained from Eq.5  
369 assuming wet conditions. The aggregate intracrystalline strain rate ( $\dot{\epsilon}_{\text{IC}}$ ) is showed for  
370 comparison (Intracrystalline). Previously reported high-temperature and low temperature  
371 flow laws for olivine polycrystals are also shown for comparison: H&K03 stands for *Hirth*  
372 *and Kohlstedt* [2003] dislocation creep law, assuming an activation volume of  $12.8 \text{ cm}^3/\text{mol}$   
373 and an hydroxyl content  $C_{\text{OH}} = 300$  ppm H/Si. Dem13 stand for *Demouchy et al.* [2013], and  
374 Rate04 for *Raterron et al.* [2004]. See text for further explanation. The effect of intergranular  
375 strain relaxation mechanism is apparent through the reduction of viscosity by a factor of  $\sim 100$   
376 (solid lines) at shallow depths relative to that obtained from the classical *Hirth and*  
377 *Kohlstedt's* flow laws or laws based on intracrystalline deformation (dashed lines). Do note,  
378 however, that such effect is probably reduced in the mantle because of larger grain sizes than  
379 in experiments. At deeper depths, the difference between the present law and that of *Hirth and*  
380 *Kohlstedt* [2003] is due to the pressure-induced change of dominant slip system in olivine.

381

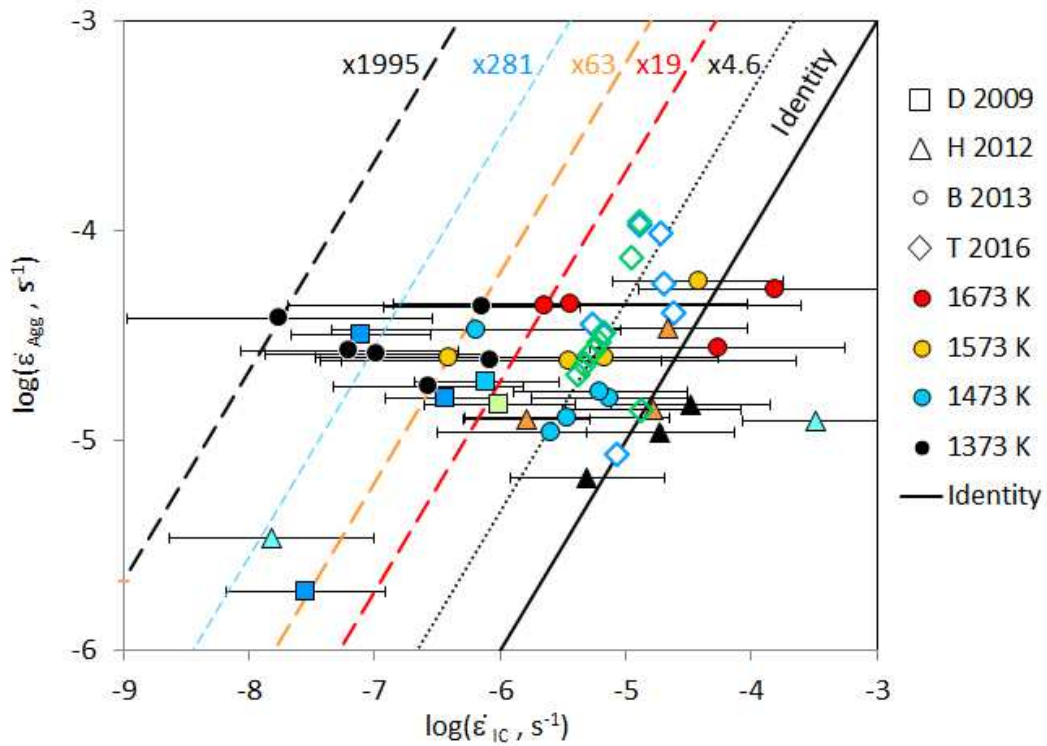
382 **Figure 1**

383



384

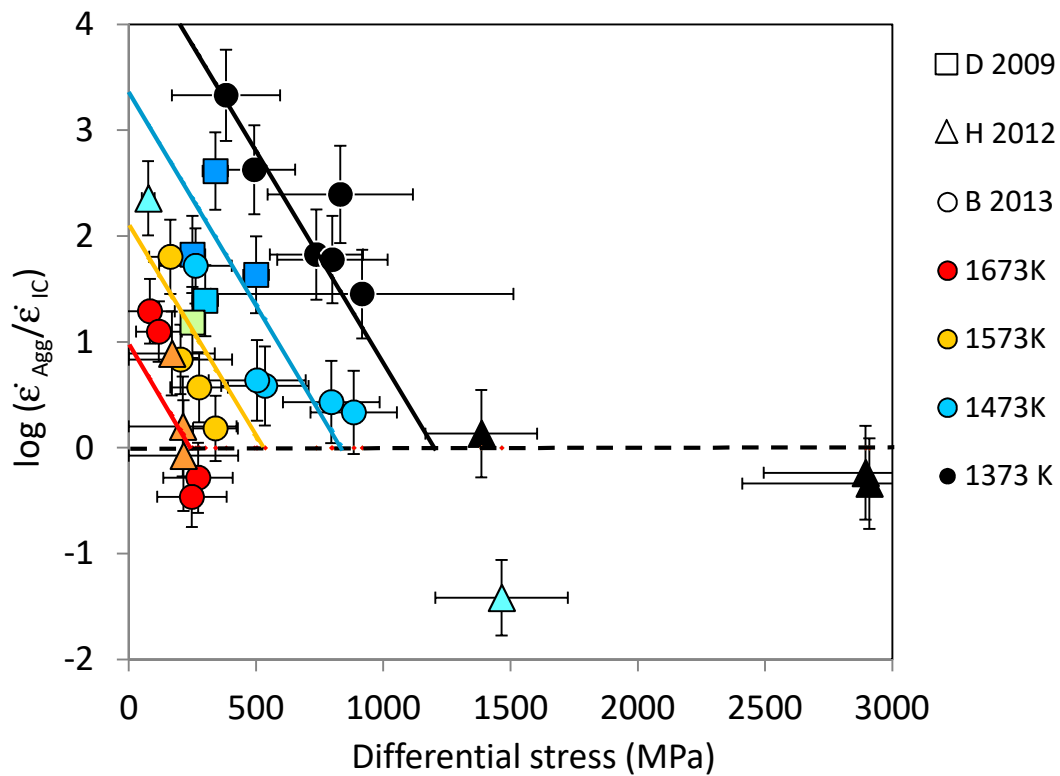
385 **Figure 2.a**



386

387

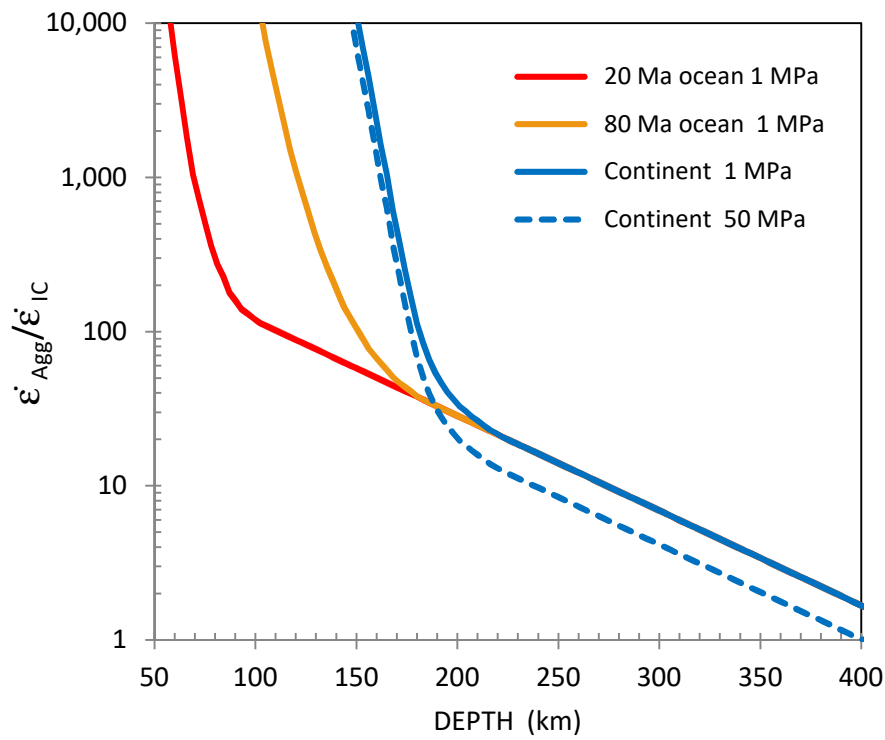
388 **Figure 2.b**



389

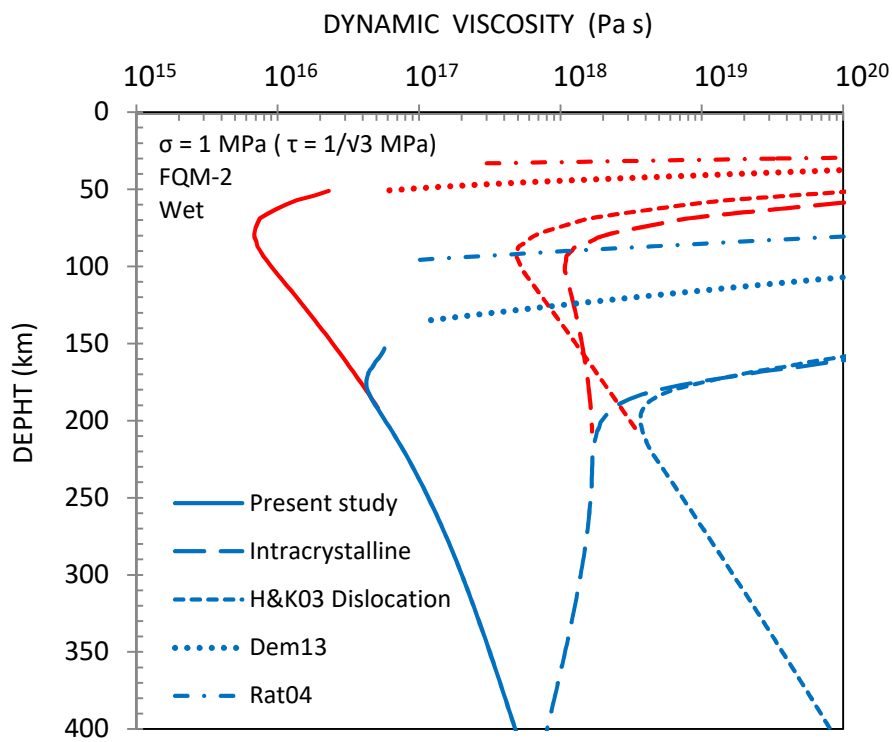
390

391 **Figure 3.a**



392

393 **Figure 3.b**



394